ROYAL SOCIETY
OF CHEMISTRY

PAPER

Check for updates

Laser-drilled functional wood materials show improved dimensional stability upon humidity changes – a neutron imaging analysis†

Yong Ding, [iD] ‡*[ab] Mahdieh Shakoorioskooie,‡[c] David Mannes,[c] Zhidong Zhang, [iD] [d] Dmitry Chernyshov [iD] [e] and Ingo Burgert [iD] [ab]

Wood and wood-based composites are increasingly studied because of their potential to regulate indoor humidity through moisture exchange with the air. Understanding their dimensional stability under fluctuating moisture conditions is essential for uncovering the underlying mechanisms and their practical use. This study employed neutron imaging to elucidate the moisture dynamics within wood materials under varying relative humidity conditions. High-resolution and *in situ* golden ratio tomography provided insights into moisture distribution and dimensional changes within the wood. Affine and non-affine registration techniques identified both the global and local deformations, highlighting dimensional instability in native wood and its improvement through laser drilling. Structural modification by laser drilling processes is effective in improving the moisture transport speed in wood and limiting dimensional changes. Moreover, the laser-drilled wood provides a highly feasible scaffold for further chemical modifications. Coating the cell lumina surface of laser-drilled wood with MOFs results in remarkably high moisture sorption capacity and improved dimensional stability compared to native wood and laser-drilled wood. The MOF layer acts as a barrier during water adsorption and as a reservoir during desorption. This study presents a promising strategy for the development of high-performance wood materials that leverage wood's inherent benefits while overcoming some current limitations.

1 Introduction

Wood is a renewable and carbon-storing material that has garnered significant attention because of its potential in sustainable applications. Its hierarchical porous structure and lignocellulosic composition make it an excellent candidate for engineering highly functional materials through chemical treatments and processing techniques.[1–7] These processes enhance the inherent properties of wood, making it suitable for a wide range of applications. Specifically, wood's multiscale pores provide favorable pathways for directed multiphase transport of molecules, gases, and liquids. This characteristic makes wood-based composites highly promising for water

transport related applications,[8–10] such as atmospheric water harvesting,[11,12] wastewater treatment,[13] and seawater desalination.[14,15] Among them, utilizing wood for autonomous indoor humidity regulation has gained increasing attention with the ambition to reduce energy consumption and carbon footprint in the building sector due to the global warming challenge.[16–18]

Wood can be used to regulate relative humidity (RH) by exchanging moisture with the surrounding air. However, native wood's humidity regulation capacity is limited due to its low moisture sorption capacity and slow moisture exchange rate. To address this, researchers have focused on enhancing wood's water-sorption ability through chemical and structural modifications.[19–23] For instance, Ran *et al.* developed a wood modification strategy combining deep eutectic solvent (DES) impregnation of cell walls with heat treatment.[24] This method significantly enhanced the wood's water-holding capacity, resulting in a 2.5-fold increase in the moisture buffer value compared to native wood. DES modification also improved wood's hygroscopicity while limiting cell wall expansion, offering an effective strategy for balancing moisture adsorption and dimensional stability.

In previous work by the authors, Ding *et al.* reported a process to improve the responsiveness of wood to humidity changes by laser-drilling microscopic holes to cut open wood fibers.[25,26] The laser drilling process improved the accessibility

[a]Wood Materials Science, Institute for Building Materials, ETH Zürich, 8093, Zürich, Switzerland. E-mail: yoding@ethz.ch

[b]WoodTec Group, Cellulose & Wood Materials, Empa, 8600 Dübendorf, Switzerland

[c]Laboratory for Neutron Scattering and Imaging, PSI Center for Neutron and Muon Sciences, Forschungsstrasse 111, 5232 Villigen, Switzerland

[d]Durability of Engineering Materials, Institute for Building Materials, ETH Zurich, 8093 Zurich, Switzerland

[e]Swiss-Norwegian Beam Lines at European Synchrotron Radiation Facility, 71 Avenue des Martyrs, Grenoble 38043, France

† Electronic supplementary information (ESI) available. See DOI: https://doi.org/10.1039/d4ta07564a

‡ Contributed equally.

of wood porosity, allowing for efficient chemical modification. Subsequent modifications, such as impregnating the cell walls with hygroscopic salts like calcium chloride[25] or cell wall coating with porous metal–organic frameworks (MOFs),[26] further increased the wood's moisture sorption capacity and response rate. These studies demonstrated the potential of wood-based composites for effective indoor humidity regulation by enhancing their ability to exchange moisture with the surrounding environment. While these modifications significantly improve wood's hygroscopic properties, the swelling and shrinking of wood as it absorbs and desorbs water can lead to dimensional instability.[27] Dynamic changes in moisture content can induce deformation, which may compromise performance and lead to structural failure.[28–32] Therefore, understanding the relationship between moisture uptake and dimensional changes at the tissue level is essential for developing reliable wood-based materials for humidity regulation.

In this study, we aim to deepen our understanding of how moisture uptake affects the dimensional stability of wood after structural and chemical modification sequence treatments under dynamic humidity conditions. Neutron imaging emerges as a powerful, non-destructive, and high-resolution tool for studying moisture transfer processes in wood. Neutrons are particularly sensitive to "light" elements such as hydrogen, making this technique ideal for investigating moisture transport in hygroscopic materials like wood.[33–37] Previous work reported by Mannes *et al.* utilized neutron imaging to study the moisture diffusion processes in wood and to quantify the water content within wood samples.[36] Due to the high sensitivity of neutron imaging for hydrogen, small amounts of water (*e.g.* by adsorption from air moisture) can be detected and quantified. Notably, neutron imaging allows high resolution tracing of not only the time-dependent diffusion processes but also the spatial moisture distribution within the specimens.[38,39] Therefore, we envisage neutron imaging as a well-suited technique to study the moisture distribution and dimensional change of the functional wood samples under dynamic humidity conditions. Systematic studies on the moisture distribution and its coupling with dimensional changes of the developed wood composites can provide valuable guidance in designing functional wood-based materials for applications such as indoor humidity regulation.

The cutting-edge neutron imaging technique allows for a detailed examination of the moisture dynamics within the modified wood materials. Specifically, we conducted golden ratio (*in situ*) tomography of wood samples under varying conditions of R.H.[40] This method allowed us to perform high-resolution, time-series tomography, obtaining detailed insights into moisture distribution and transport within the wood. Additionally, advanced affine and non-affine image registration methods were used to pinpoint global and local deformations in the different wood materials. This approach provides further insight into the interplay between moisture content and wood's physical properties at the microstructural level, enabling us to assess how laser drilling and subsequent chemical modifications influence dimensional stability.

2 Methods

2.1 Materials preparation

2.1.1 Native wood. Poplar wood (*Populus tremula*) tangential sections with the dimensions of 50 mm × 50 mm × 1.5 mm ($L \times T \times R$) were cut with a circular saw. $T \times L \times R$ represents Tangential × Longitudinal × Radial directions.

2.1.2 Lasered wood. A commercial 10.6 μm CO_2 laser engraver (Speedy 300, Trotec) was used to perform a structural modification of native wood, named lasered wood. The power of the laser beam was 20 W, the scan rate was 2.5 mm s^{-1}, and the image density was 1000 pulses per inch. The defocus distance was zero.[41]

2.1.3 MOF/wood. Chemical modification was performed after the laser processing. MIL-101(Cr) MOF powder was first synthesized based on a previously reported method.[26,42] Then, the MIL-101(Cr) MOF powder was dispersed in ethanol solution to obtain a MOF solution with a concentration of 10 g L^{-1}. In a subsequent step, the lasered wood samples were impregnated in the MOF solution for 12 h at room temperature under gentle stirring. The composite was then dried at 103 °C for 12 h. This was a typical procedure of one impregnation cycle, which was repeated 15 times. We named the final sample MOF/wood.

2.2 Materials characterization

MOF loading: 10 specimens with the dimensions of 10 mm × 10 mm × 1.5 mm ($L \times T \times R$) were cut out from 50 mm × 50 mm × 1.5 mm specimens and used (Fig. S1†). The MOF loading was calculated using the formula:

$$\text{MOF loading} = (m_1 - m_0)/m_0$$

where m_0 represents the initial weight of the laser drilled wood and m_1 represents the specimen mass after MOF impregnation treatment.

Bulk density: 10 specimens with the dimensions of 10 mm × 10 mm × 1.5 mm ($L \times T \times R$) were used (Fig. S1†). The bulk density was calculated using the formula:

$$\rho = \text{mass/volume}$$

The morphology of the samples was characterized using a scanning electron microscope (SEM; FEI Quanta 200F, Hillsboro, OR, USA). A Pt–Pd (80/20) coating of ∼10 nm thickness was applied to the samples with a sputter coater (CCU-010, Safematic, Switzerland).

Dynamic water vapor adsorption and desorption were measured using an automated sorption balance device (DVS Advantage ET85, Surface Measurement Systems Ltd). Ten milligrams of each sample were first dried for 10 h at 60 °C and at a partial water vapor pressure of $p/p_0 = 0$. The measurement was carried out with ascending p/p_0 steps of 0, 0.10, 0.25, 0.45, 0.65, 0.80, and 0.95 for adsorption and then with descending steps in the same manner for desorption at 25 °C. Equilibrium in each step was defined to be reached at a mass change per time ($\text{d}m/\text{d}t$) of less than 0.0005% per min over a 10 min period or a maximal

This journal is © The Royal Society of Chemistry 2025

J. Mater. Chem. A, 2025, **13**, 6364–6375 | **6365**

time of 1000 min per step. The samples were exposed to a flow rate of 200 sccm, and the carrier gas used was N_2.

X-ray diffraction (XRD) was performed at BM01 (SNBL/ESRF in Grenoble, France) using the PILATUS@SNBL diffractometer.[43] The monochromatic beam ($\lambda = 0.72325$ Å) and the parameters of the detector were calibrated on the LaB6 NIST 660b reference material.[44] The obtained calibrations were implemented in Bubble for further azimuthal integration of 2D images.

2.3 Neutron imaging

Neutron imaging was carried out in the second position of the ICON cold neutron imaging facility at the Swiss spallation neutron source (SINQ) at the Paul Scherrer Institute (PSI). Radiographic acquisition was conducted using an iKon-L CCD camera (Andor Technology) coupled with a neutron-sensitive 30 μm thick Gadox scintillator, covering a field of view of 70×70 mm². During the entire measurement, the temperature of the climate chamber was fixed at 25 °C. Two types of tomography were carried out: the ordinary (normal) neutron tomography (O-tomography) and high-frequency Golden Ratio tomography (GR-tomography).

2.3.1 Sample setup. A dedicated climate-controlled sample environment was used,[34] including a custom-designed sample holder with perforated shelves of aluminum to support the samples, while not restricting their free expansion/shrinkage (Fig. 1). Specimens with a diameter of 9 mm were cut out from 50 mm $\times$ 50 mm $\times$ 1.5 mm specimens for neutron imaging investigation (Fig. S1†). Before the tests, all specimens were climatized at 25 °C and 25% RH for 7 days. The sample environmental conditions were preserved inside a climate chamber with controlled temperature and humidity levels throughout the *in situ* tomography measurements.[45] The entire climate chamber is made of aluminum, which is almost transparent to neutrons.

2.3.2 O-tomography. O-tomography was carried out in two equilibrium states of the samples. The test conditions were set
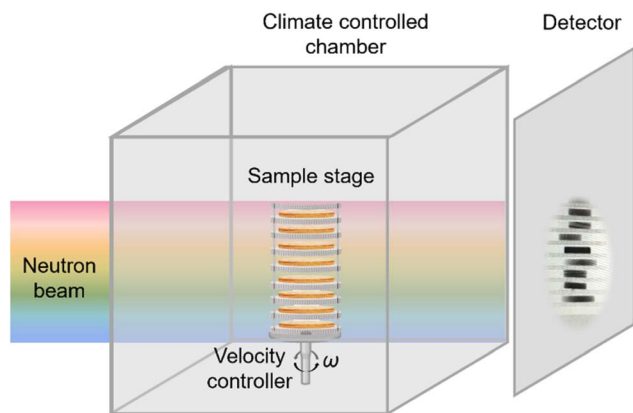

Fig. 1 Sample environment setup for *in situ* tomography measurements. The setup included aluminum perforated shelves designed to support samples while allowing unrestricted expansion and shrinkage. This sample holder was housed within a climate-controlled chamber.
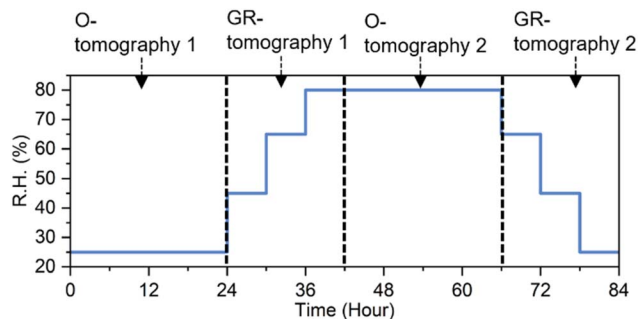

Fig. 2 The set ambient humidity profile for tomography scenarios.

at 25% R.H. for 24 hours for the first measurement, namely the dry stage. The first GR-tomography followed the dry stage. Afterward, the wood specimens were conditioned at 80% R.H. for 24 hours to perform the second high-resolution O-tomography, namely the wet stage (Fig. 2). A total of 1125 projections (angles) with a pixel size of 32.327 μm were acquired, over 360° during O-tomography with an exposure time of 70 s. The set R.H. and real R.H. during measurement are shown in Fig. S2.†

2.3.3 GR-tomography. GR-tomography is a technique that improves conventional tomography by acquiring images at projection angles based on the golden ratio, approximately 137.5°. Instead of using equally spaced angles, which is common in traditional approaches, the GR-tomography method selects angles that are irrationally spaced. This method is especially useful for imaging dynamic processes. The irregular spacing of the projection angles helps to capture the structural changes at a higher temporal resolution. To acquire high-frequency imaging while cycling the R.H. inside the climate chamber, we employed GR-tomography to capture the dynamic hygroscopic behavior of wood between two O-tomography steps. This technique enabled us to monitor the moisture distribution and dimensional changes of wood samples with high spatial and temporal resolution.[40] Humidity levels used during the first GR-tomography were 45%, 65%, and 80%, with a conditioning time of 6 hours for each humidity level. The humidity level for the second GR-tomography step was the reverse of the previous steps, namely 65%, 45%, and 25%, with the same conditioning time of 6 hours. This measurement was designed to test the dynamics of water sorption. The exposure time for GR-tomography was set to 35 s.

Two GR-tomography steps were carried out to investigate the water adsorption process (GR-1) and the water desorption process (GR-2). The R.H. levels of the sample environment and duration are shown in Fig. 2 and S2.†

2.3.4 Image reconstruction. All tomographic reconstructions were carried out using MuhRec software based on a parallel beam, filtered back projection (FBP) algorithm.[40] The procedure for tomogram reconstruction optimization for GR-tomography is shown in ESI (Fig. S3†). Tomographic reconstructions were carried out every 80 minutes, resulting in a total of 13 tomograms covering all conditioning steps for each GR-tomography step, enabling the close monitoring of the dynamic moisture interactions within the wood samples.

6366 | *J. Mater. Chem. A*, 2025, **13**, 6364–6375

This journal is © The Royal Society of Chemistry 2025

2.3.5 Image processing. To quantitatively assess the global and local deformations in the wood samples subjected to adsorption and desorption processes, we implemented a comprehensive image registration strategy utilizing both affine and non-affine transformations based on B-splines. The registrations were carried out using the SimpleElastix library based on a mutual information metric.[46,47]

2.3.5.1 Affine image registrations for global wood deformation analysis. Affine registration was carried out to compute the global volumetric expansions or contractions due to moisture interaction. The affine transformation model is a combination of rotation, shear, isotropic scaling, and translation, mathematically expressed as:

$$I_{AFF}(t_i) = A \cdot I(t_i) + b$$

$I_{AFF}(t_i)$ is the moving image transformed under affine registration at time t_i with respect to the fixed image $I(t_0)$; A is a 3×3 matrix representing rotation, scaling, and shear; b is a translation vector; $I(t_i)$ is the moving image at time t_i.

The Jacobian matrix, $J_{\vec{T}}(\vec{x}, t_i)$, of a transformation function is a tool to describe how a function maps points from one space to another and how the function changes locally in terms of scaling, rotation, and distortion. The Jacobian matrix, $J_{\vec{T}}(\vec{x}, t_i)$, provides a scalar value that represents the effect of the transformation at a point in terms of volume change. The determinant of the Jacobian matrix for the affine transformation, $J_{\vec{T}_{AFF}}(\vec{x}, t_i)$, indicates global volumetric changes between the reference and moving images. If the Jacobian determinant is larger than one, it means that there is an expansion at that point of the image (sample); if it is less than 1, it implies shrinkage, and if it is equal to 1, it means no changes in the volume.

2.3.5.2 Non-affine image registrations for local wood deformation analysis. We employed a non-affine transformation for analyzing local deformations. This model offers the possibility to map intricate local changes, mathematically expressed as:

$$I_{N-AFF}(t_i) = B(I_{AFF}(t_i), \phi)$$

$I_{N-AFF}(t_i)$ represents the image after applying a non-affine transformation to the affinely transformed image $I_{AFF}(t_i)$, relative to the fixed image $I(t_0)$. B is the B-spline function used for the transformation, and ϕ denotes the set of B-spline coefficients that define local deformations. The deformation vector field (DVF), $\vec{u}_{N-AFF}(\vec{x}, t_i)$, was used as a vector field. $\|\vec{u}_{N-AFF}\|(\vec{x}, t_i)$ measures the magnitude of deformation at each point of the image. The determinant of the Jacobian matrix for the non-affine transformation matrix, $J_{\vec{T}_{N-AFF}}(\vec{x}, t_i)$, provides insight into the local volumetric changes.

2.3.5.3 Water volume fraction estimation. To determine the variations of the water volume fraction within the wood samples, we performed an analysis between the non-affine registered images at each timepoint, $I_{N-AFF}(t_i)$, and the reference image taken under the baseline conditions, $I(t_0)$. This process aimed to estimate the changes in water content within the wood samples over time, compared to the reference state. The differential image, $\Delta I(t_i)$, contains voxel values representing the increase or decrease in attenuation, which can be directly related to changes in water content within the sample. By integrating these changes over the entire volume of the sample, we calculated the total change in water volume within the sample at each time point. To express these changes as a fraction of the total volume of the wood (segmented at the reference state), the change in water volume was then divided by the entire volume of the wood sample. This yields the volume fraction of water or moisture variation inside the samples compared to the reference conditions:

$$\text{Moisture fraction}(t_i)\% =$$

$$\frac{\text{volume change due to the water dynamics}(\Delta I(t_i))}{\text{total volume of the wood}} \times 100$$

The differential analysis provides a statistical measure of the wood's water content changes in response to varying R.H. conditions.

3 Results

3.1 Morphology and composition of samples after the sequential treatments

Native wood features a directional porous structure. Native poplar wood's axial tissue is mainly composed of vessels and fibers, with lumina diameters between 60–100 μm and 5–15 μm, respectively (Fig. 3a and b). In this study, we performed structural modification with a laser drilling process perpendicular to the fiber direction to cut open wood fibers (lasered wood). The diameter of laser-drilled channels was approximately 200 μm. The morphology of the lasered wood is shown in Fig. 3c and d. The laser drilling process predominantly removed wood components due to the high laser energy absorption efficiency of cellulose and created artificial channels perpendicular to the fiber direction, resulting in a 3D interconnected porous structure.[48] Because of laser drilling, the density decreased from 403.3 ± 21.0 kg m^{-3} to 340.8 ± 40.3 kg m^{-3}. We further modified the laser-drilled wood scaffold with MOF MIL-101(Cr) particles. MIL-101(Cr) was chosen because of its high water sorption capacity and its ability to regulate moisture effectively within the recommended R.H. range.[49–58] Subsequent impregnation with MIL-101(Cr) particles resulted in a MOF loading of 15.25 ± 1.22 wt%. The density of the MOF/wood composite was calculated to be 373.7 ± 28.1 kg m^{-3}. The SEM images (Fig. 3e–h) show that the inner cell lumina surfaces were coated with a dense layer of MOF particles. X-ray diffraction measurement confirmed the presence of a MOF MIL-101(Cr) layer with a crystal structure corresponding to the pure MOF, indicating the successful impregnation of the wood structure (Fig. S4†).

3.2 Wood–moisture interaction at the tissue level

With the sequential treatments of the laser drilling process and MOF modification, we obtained three samples for comparison: native wood, lasered wood and the MOF/wood composite. The comprehensive investigation of their moisture interaction on
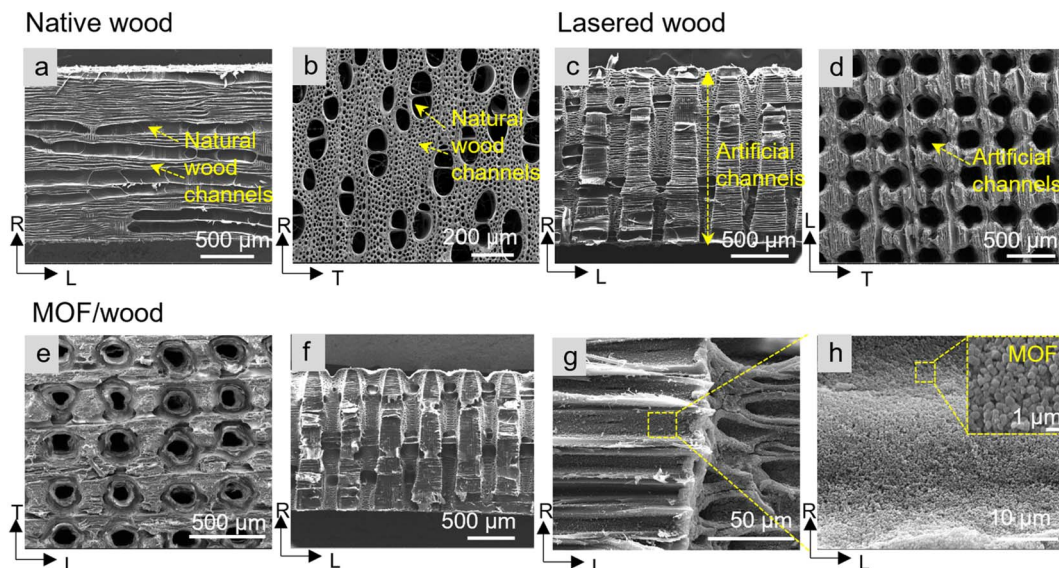
This journal is © The Royal Society of Chemistry 2025

J. Mater. Chem. A, 2025, **13**, 6364–6375 | **6367**

Fig. 3 Morphology of native wood, lasered wood, and MOF/wood. (a and b) SEM images of native wood from different planes. (c and d) SEM images of lasered wood showing the creation of artificial channels by laser drilling from different planes. (e–h) SEM images of MOF/wood. (e) and (f) show that MOF deposition does not block the laser-drilled channels. (g) and (h) shows that a dense layer of MOF MIL-101(Cr) was deposited on the cell wall surface.

the microscale includes sorption isotherms, moisture transport, and global and local swelling/shrinkage.

3.2.1 Water sorption isotherms. Dynamic water vapor sorption (DVS) measurement represents a powerful tool for characterizing the interaction of water vapor with hygroscopic materials like wood. Water sorption isotherms from DVS measurements showed that native wood and lasered wood had a mass change of 19.68% and 18.65%, respectively, indicating that the laser drilling process did not significantly influence the water sorption capacity of the wood (Fig. 4a). MOF/wood showed a mass change of 35.10%, two times higher than that of native wood. The most significant change happened in the range of 25–65% R.H., where MOF/wood starts to take up high amounts of moisture. In the R.H. ranges of 0–25% and 65–80%, native wood, lasered wood, and MOF/wood showed similar sorption behavior. The MOF/wood had the highest hysteresis at 45% R.H. (Fig. 4b).[59,60]

3.2.2 Moisture transport dynamics. The water isotherms from DVS measurements provide insight into the wood–water interactions, especially the moisture uptake capacity and hysteresis. For applications such as indoor humidity regulation, it is important to understand the moisture uptake dynamics as well as the associated dimensional changes, which were studied by neutron imaging.

We first carried out moisture fraction analysis using GR-tomography measurements, which allowed us to study the dynamics of moisture adsorption/desorption of the produced wood materials. Fig. 5a illustrates the dynamics of moisture fraction changes during the water adsorption process from GR-1 for native wood, lasered wood, and MOF/wood at varying humidity levels. After 6 hours at 45% R.H., the moisture volume fraction of the native wood remained stable at ∼10.16%. When

the R.H. was increased to 65% for another 6 hours, the moisture fraction rose to 13.43%. When the R.H. was increased to 80% for another 6 hours, the moisture content further increased to 20.02%. Similarly, lasered wood exhibited a stable moisture fraction of ∼15.80% at 45% R.H. and then increased to the 17.85% moisture fraction at 65% R.H. By the end of the third stage at 80% R.H., lasered wood achieved a moisture fraction of 23%. MOF/wood showed distinct behavior in moisture uptake. At 45% R.H., after 6 hours, the moisture fraction was stable at ∼21.28%. As the humidity increased to 65% R.H., the moisture
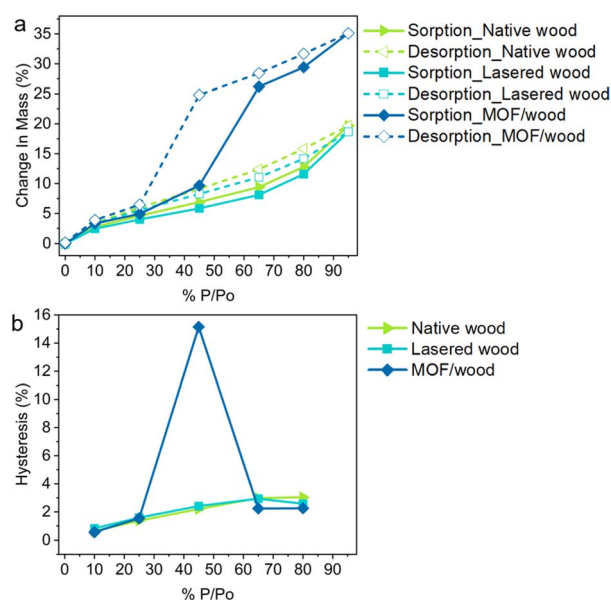

Fig. 4 (a) Water sorption isotherms and (b) hysteresis of native wood, lasered wood and MOF/wood.

6368 | *J. Mater. Chem. A*, 2025, **13**, 6364–6375

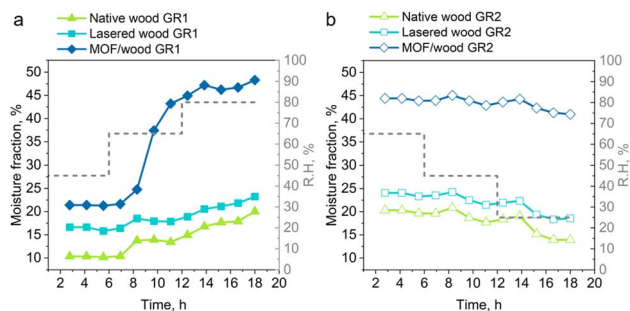This journal is © The Royal Society of Chemistry 2025

Fig. 5 Comparative analysis of the moisture transport dynamics in the wood materials with GR tomography. (a) Moisture mass fraction change in GR 1 during the water adsorption/wetting stage. (b) Moisture mass fraction change in the GR 2 during the water desorption/drying stage. Moisture mass fraction was estimated as the fraction of segmented moisture, derived from differential analysis between the golden-ratio (GR) tomograms of the samples at each time point compared to the initial GR tomogram.

fraction significantly increased to 43.20%. Finally, at 80% R.H., MOF/wood's moisture content further increased to 48.29%. Fig. 5b depicts the moisture loss dynamics during the water desorption process from GR-2. Both native wood and lasered wood exhibited gradual declines in moisture content at 65% and 45% R.H., with the most notable decrease occurring at 25% R.H. Similarly, MOF/wood showed slow moisture release at 65% and 45% R.H., with a more rapid decrease at 25% R.H. After the GR-2 measurement, MOF/wood had a moisture fraction loss of

3.44%, which was lower than that observed in native wood and lasered wood.

3.2.3 Moisture-induced swelling/shrinkage. Dimensional changes are closely associated with wood–moisture interactions. Fig. 6 and S5–S7† capture the dynamics of global volumetric expansion/shrinkage in the native wood, lasered wood, and MOF/wood samples during the process of adsorption and desorption, respectively. The chart distinctly illustrates the global volumetric change over time, marked by the tracking of GR-tomography 1 and GR-tomography 2. The surrounding visualization images at different time points showcase both the Jacobian determinant and the displacement vector fields, revealing the moisture-induced local deformations within the wood. Both the global volumetric change and the local deformations are crucial for understanding the wood's dimensional changes upon moisture content changes. Building upon the analysis illustrated in Fig. 6, moisture fraction analysis and dimension change analysis can be combined. This allows us to not only observe the dimensional expansion and shrinkage but also to correlate these changes directly with water uptake across the samples. Through this approach, we aim to gain a comprehensive understanding of the implications of each modification on the wood's dimensional changes in response to humidity changes.

3.2.3.1 Global dimensional changes from GR-tomography. The global volumetric change refers to the overall change in the volume of the wood sample. This computation was done through an affine registration, where the entire image of the
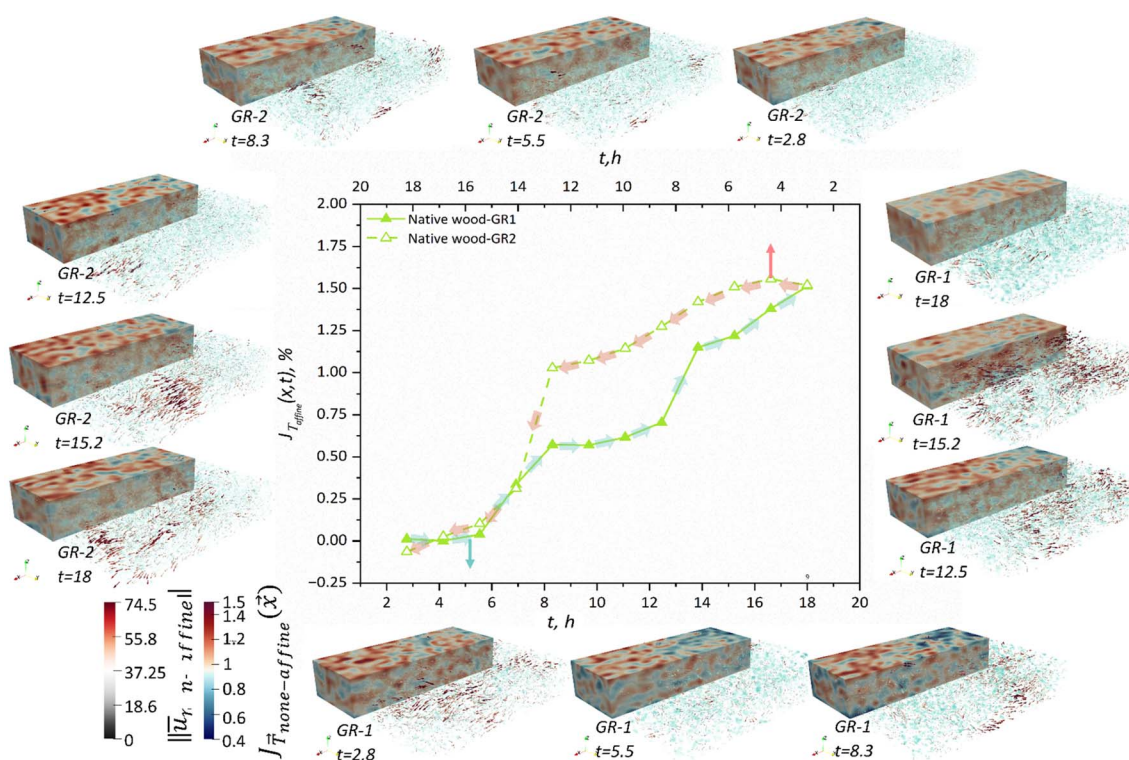

Fig. 6 Illustration of the dynamics of volumetric expansion/shrinkage in native wood during the GR1 and GR2 tomography steps, with additional demonstrations of the local deformations and water transport dynamics occurring simultaneously alongside the global volumetric changes, at different time points.

This journal is © The Royal Society of Chemistry 2025

J. Mater. Chem. A, 2025, **13**, 6364–6375 | **6369**

wood sample is transformed uniformly to match the reference state. The affine transform adjusts the image globally using scaling, rotation, and translation, without accounting for local variances within the sample. The determinant of the Jacobian matrix from this transformation, $J_{\vec{T}_{AFF}}(\vec{x}, t_i)$, gives a scalar value representing the factor by which the volume has changed. This global affine registration helps assess the overall behavior of the material.

Fig. 7a shows the dynamics of volume change during the water adsorption process (GR-1) for native wood, lasered wood, and MOF/wood at different humidity levels. Native wood exhibited almost no volume change (0.04%) after 6 hours at 45% R.H. When the R.H. increased to 65% and was held there for another 6 hours, the native wood started to swell linearly and reached a volume change of 0.62% after 6 hours at 65% R.H. and a final volume change of 1.51% after 6 hours at 80% R.H. Lasered wood demonstrated steady swelling across all humidity stages. At the end of GR1, lasered wood showed a volume swelling of 1.30%, which is less than that of native wood. MOF/wood exhibited distinctly low volume changes and dynamics at each humidity level. It showed minor dimensional changes at 45% and 65% R.H. The volume change of MOF/wood was only 0.03% after 6 hours at 45% R.H. and 0.10% after another 6 hours at 65% R.H., significantly lower than that of both native wood and lasered wood. When the humidity increased to 80%, MOF/wood finally started to exhibit a nearly linear increase in volume and reached a volume change of 1.05%, which was still lower than that of native wood and lasered wood.

Fig. 7b presents the dynamics of volume changes during the water desorption process (GR-2). Both native wood and lasered wood showed gradual shrinkage as the relative humidity was lowered. The most significant shrinkage occurred at 25% R.H. for both samples. MOF/wood also demonstrated a non-smooth shrinking behavior, similar to lasered wood. In comparison, lasered wood and MOF/wood had a lower overall volume change compared to native wood in both water adsorption and desorption processes, indicating improved stability across

varying humidity levels. MOF/wood displayed the lowest volume changes at all stages, showcasing its superior performance in minimizing dimensional changes.

3.2.3.2 Local dimensional changes from O-tomography. Non-affine registration enabled us to map local deformations, which cannot be captured by the affine transformation. For instance, although nearly no global volume change was observed for native wood in the first 6 hours during GR-1 (Fig. 6), the displacement vector field visualization images at 2.8 h and 5.8 h show local changes. Non-affine registration allows for local variations in the transformation parameters, which allows us to record local expansions or contractions in different parts of the wood sample. The local deformation details are crucial for understanding how moisture affects the wood at a microscopic level, highlighting areas of stress concentration, differential swelling, or other heterogeneities. We carried out non-affine registration of three samples using the first and the second O-tomography data. The first O-tomography serves as our reference condition (*e.g.* the dry state after conditioning at 25% R.H.). By relating the second O-tomography (*e.g.* the wet state when conditioning at 80% R.H.) to the reference image, we can obtain important information about local dimensional changes after stabilizing at 80% R. H. (*e.g.* the wet state). The local deformations of the three samples, namely the native wood, the lasered wood, and the MOF/wood sample, are compared in Fig. 8. Fig. 9 illustrates the moisture-induced deformation in wood samples by presenting the same sets of data as Fig. 8 but in a 3-dimensional (3D) format. This 3D visualization allows for a more comprehensive perception of the spatial relationship between deformation and the wood's structure.

Each row corresponds to a different type of wood sample, while each column represents a unique aspect of the study designed to elucidate the interaction between wood and moisture. The first column (Fig. 8a, e and i) displays tomograms with superimposed deformation vector fields $\vec{u}_{N\text{-AFF}}(\vec{x}, t_i)$, allowing for the visualization of the local deformation magnitude and orientation. This illustrates the direction and magnitude of deformation across the sample, providing insight into the effect of each type of treatment on the wood's response to moisture. The second column (Fig. 8b, f and j) shows the water distribution within the samples, with the deformation vectors $\vec{u}_{N\text{-AFF}}(\vec{x}, t_i)$ overlaid to correlate moisture patterns with physical changes. This is critical for understanding how water uptake or release corresponds to the wood's deformation, essentially connecting the hygroscopic behavior to the physical response. In the third column (Fig. 8c, g and k), the norm of the deformation field, $\|\vec{u}_{N\text{-AFF}}\|(\vec{x}, t_i)$, is shown, highlighting the intensity of deformation without directional influence as a continuous map. This serves to highlight the areas most affected by moisture interaction, which is particularly useful for assessing the effectiveness of the treatment in distributing the mechanical stress caused by swelling or shrinking. The fourth column (Fig. 8d, h and l) presents the determinant of the Jacobian maps, $J_{\vec{T}_{N\text{-AFF}}}(\vec{x}, t_i)$, providing a quantitative measure of local volumetric changes due to moisture absorption.
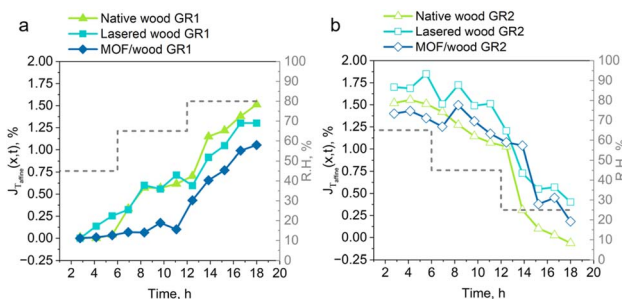

Fig. 7 Global dimensional changes of the wood materials with GR tomography. (a) Volume change in GR 1 during the water adsorption/wetting stage. (b) Volume change in GR 2 during the water desorption/drying stage. The volume change analysis is based on the determinant of the Jacobian of the affine transformation function, $J_{\vec{T}_{affine}}(\vec{x}, t_i)$, which quantifies volume–change fractions (%). This is calculated through the global affine registration of each sample's neutron golden-ratio (GR) tomograms at various time points (t_i) relative to the initial tomogram (t_1) for each forward and backward GR tomography session.
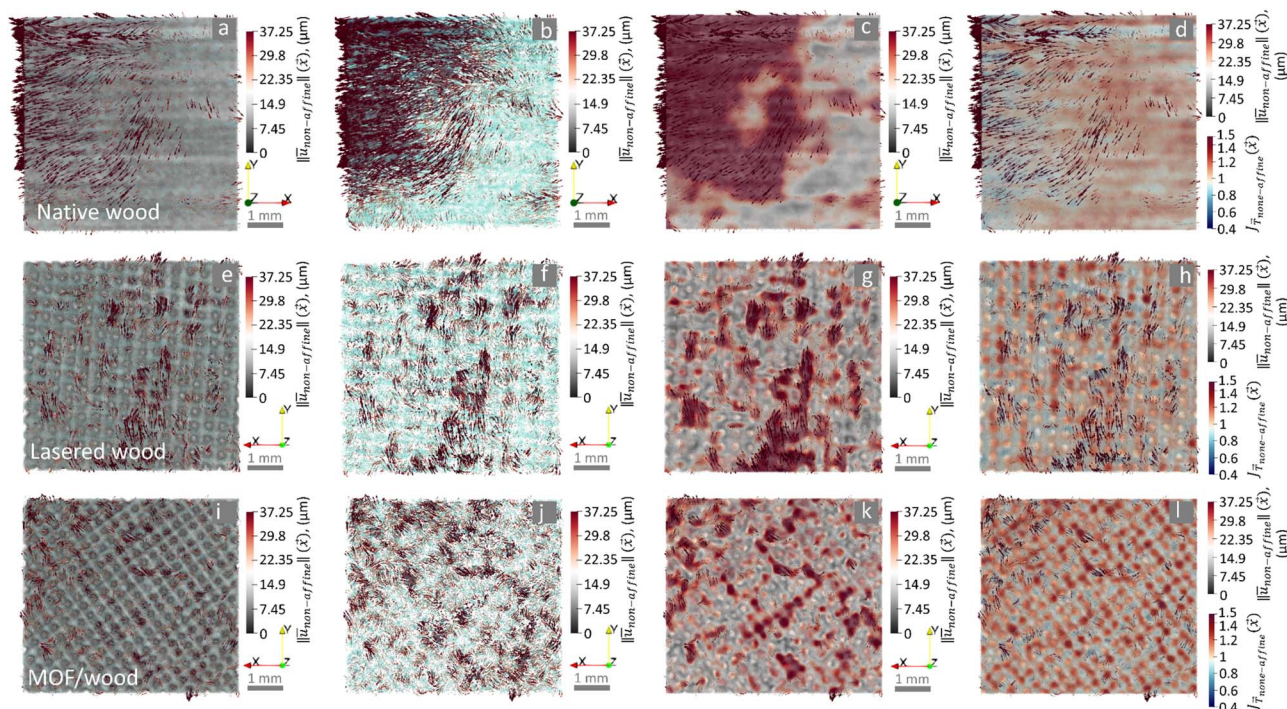
Fig. 8 2D visualization of native wood, lasered wood, and MOF/wood, respectively, from the non-affine registration of samples' neutron normal tomograms before and after exposure to wetting steps (stepwise increasing of the RH): (a, e and i) the reconstructed wood sample superimposed by water and the displacement vector field (DVF); (b, f and j) only the water distribution and $\vec{u}_{\text{N-AFF}}$; (c, g and k) superimposed map of the magnitude of the DVF, $\|\vec{u}_{\text{N-AFF}}\|(\vec{x})$, along with the DVF vectors on the wood; and (d, h and l) superimposed spatial map of the determinant of the Jacobian transformation function (volume-change fraction) $J_{\vec{T}_{\text{N-AFF}}}(\vec{x})$. The DVF represents the displacement of points from their original position in the fixed image (first-time point) to their new position in the moving or registered image (second-time point). The $J_{\vec{T}_{\text{N-AFF}}}(\vec{x})$ represents a scalar field describing the local volumetric change at each point. The values greater than one at a point indicate local expansion, while values less than one show local shrinkage (for instance, a value of 0.8 represents 20% local shrinkage. When the determinant value is exactly one, there is neither local expansion nor contraction).
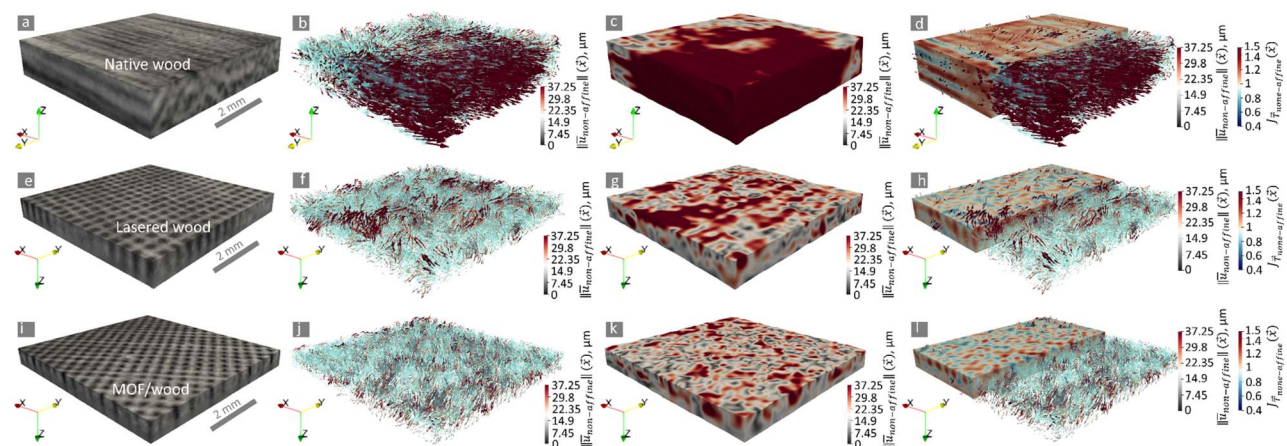

Fig. 9 Three-dimensional comparative analysis across samples. This figure presents similar illustrations to those in Fig. 8 but in a three-dimensional format. Each row corresponds to a different sample (native wood, lasered wood, and MOF/wood), showcasing a detailed comparative analysis across these samples in a 3D context.

As shown in Fig. 8a–d, native wood showed a significant displacement vector field in the *X*-axis direction during swelling, indicating a strong directionality of swelling. However, this strong directionality of swelling was not observed for the lasered wood and MOF/wood. Moreover, the 'hot regions' inside the drilled holes in the Jacobian maps, $J_{\vec{T}_{\text{N-AFF}}}(\vec{x}, t_i)$, show that lasered wood and MOF/wood have pronounced local expansions in the laser-drilled channels (Fig. 8h and l); notably, MOF/Wood showed more pronounced 'hot regions' inside the drilled holes.

4   Discussion

4.1   Laser drilling process facilitates moisture exchange

The water sorption capacity of wood is strongly influenced by its chemical composition and functional groups. Fig. 4 and Table 1 show that lasered wood and native wood possess very similar water sorption capacities. Therefore, the laser drilling process can be considered as a structural modification, causing neglectable changes in chemical composition. However, when exposed to different humidity levels for 18 hours in GR-1 measurement, lasered wood showed a higher water volume fraction compared to native wood during the entire water adsorption process (Fig. 6a and Table 1). These results indicate that although native wood and laser wood have similar chemical composition, the moisture exchange speed in lasered wood is higher than that in native wood. This can be attributed to the change in porosity due to the laser drilling process. Native wood features a directional porous structure (Fig. 3). The moisture exchange perpendicular to the fiber direction is slow down by the dense cell walls. Therefore, for these small samples, moisture exchange in native wood mainly happens in fiber direction. The laser drilling process cuts open the wood fibers, resulting in an interconnected porous structure. Therefore, moisture transport in lasered wood is facilitated perpendicular to the fiber direction through the laser drilled channels.

4.2   Laser-drilled channels lead to less global dimensional changes

Moisture content changes correlate closely with dimensional changes. In the water adsorption process, lasered wood showed higher global volume expansion compared to native wood after exposure to 45% R.H. for 6 hours and 65% R.H. for 6 hours. But after being exposed to different humidity levels for 18 hours in GR-1, lasered wood had less global volume change compared to native wood (Fig. 10a). This could be due to the laser drilling process, changing how wood deforms locally when it adsorbs water. As shown in Fig. 8 and 9, the two O-tomography measurements highlight two key differences in local deformation. First, the laser drilling process can significantly change the anisotropy of swelling. Native wood showed strong swelling anisotropy, and this is attributed to the inherent anisotropic structure of wood. The laser drilling process disrupts the natural porosity and reduces the directionality in swelling of lasered wood. Second, laser-drilled channels could serve as space for local dissipation of swelling. Therefore, the global volume change of lasered wood was lower due to local expansions around the laser-drilled channels.

4.3   Laser drilling process accommodates space for further chemical modification

The laser drilling process not only modifies the wood structure but also creates space for further chemical modification. This allowed for the incorporation of MOF particles to boost moisture uptake capacity. The MOF MIL-101(Cr) used in this study is known for its high water uptake capacity.[49,53,55,61] It exhibits low water uptake at 0–40% and 60–100% R.H., but significantly

Table 1   Moisture uptake capacity, moisture volume fraction and volume change at different humidity levels of wood samples

		Native wood			Lasered wood			MOF/wood		
	R.H. %	Moisture uptake capacity from DVS,[b] %	Moisture volume fraction, %	Volume change, %	Moisture uptake capacity from DVS, %	Moisture volume fraction, %	Volume change, %	Moisture uptake capacity from DVS, %	Moisture volume fraction, %	Volume change, %
ADS[a]	45	6.91	10.16	0.04	5.84	15.81	0.25	9.67	21.28	0.03
	65	9.40	13.43	0.62	8.11	17.85	0.72	26.19	43.20	0.10
	80	12.79	20.03	1.51	11.59	23.23	1.30	29.42	48.29	1.05
DES[a]	65	12.38	19.64	1.51	11.05	23.29	1.85	28.43	43.87	1.35
	45	9.11	17.70	1.07	8.25	21.46	1.51	24.82	42.88	1.17
	25	5.99	13.91	−0.06	5.57	18.55	0.40	6.46	40.96	0.18

[a] ADS (adsorption); DES (desorption). [b] The mass change of samples at this humidity level from DVS measurement.

6372 | J. Mater. Chem. A, 2025, **13**, 6364–6375

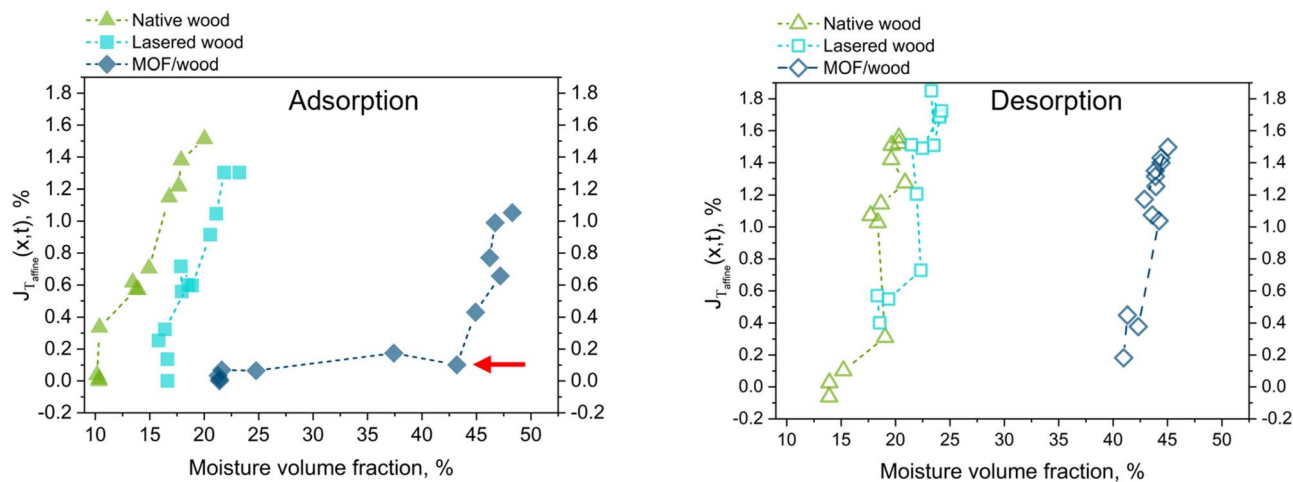This journal is © The Royal Society of Chemistry 2025

Fig. 10 Correlative analysis between the dimensional changes and moisture mass fraction in different wood specimens during GR-1 (adsorption) and GR2 (desorption).

higher uptake in the 40–60% R.H. range, resulting in steep S-shaped sorption isotherms with pronounced hysteresis in this range. As shown in Table 1, MOF/wood demonstrates notably higher moisture uptake, attributable to the unique sorption behavior of the MOFs.

The laser drilling process increases the moisture exchange speed and reduces overall dimensional changes during wood–moisture interactions. When combined with MOF coating of the inner cell walls, this leads to both high moisture uptake and the lowest volume changes (Fig. 10). During the GR-1 measurements, after 6 hours at 45% R.H., lasered wood reached a moisture fraction of 15.81% with a volume change of 0.25%. In contrast, MOF/wood had a moisture fraction of 21.28% with a significantly lower volume change of 0.03%. After exposure to 65% R.H. for another 6 hours, lasered wood showed a moisture fraction of 17.85% and a volume change of 0.72%, while MOF/wood exhibited a much higher moisture fraction of 43.20% with only a 0.10% volume change. Finally, at 80% R.H., lasered wood reached a 23.23% moisture fraction and 1.30% volume change, whereas MOF/wood showed a slight increase to a 48.29% moisture fraction and a volume change of 1.05%. At all humidity levels, the overall volume change of MOF/wood remained lower than that of lasered wood. This suggests that moisture first interacts with the MOF layer and is stored within it, contributing less to wood swelling in the time frame of the GR-1 measurements. This explains the high moisture fraction and low volume change observed at 45% and 65% R.H. stages. At 80% R.H., as the MOFs reach a high moisture fraction, water interaction with the cell walls is more pronounced, leading to cell wall expansion, which accounts for the increased volume change at this stage. During the desorption process (GR-2), MOF/wood exhibited lower moisture loss and fewer dimensional changes compared to native and lasered wood. This indicates that the MOF layer acts as a reservoir, slowing down moisture release during water desorption. Hence, partial decoupling of moisture uptake and dimensional change is effectively achieved through sequential treatments involving laser drilling and MOF coating of the cell lumina. This approach

is particularly valuable for applications requiring wood composites to maintain structural stability in environments with fluctuating humidity, such as for indoor humidity regulation.

5 Conclusions

This study employed a neutron imaging technique to *in situ* monitor the dynamics of moisture and dimensional changes in wood. *In situ* golden ratio tomography under dynamic R.H. and high precision tomography under fixed R.H. were carried out. Affine and non-affine image registration methods provided detailed insights into moisture distribution and deformations within wood materials at the tissue level under dynamic humidity levels. The results revealed that the laser drilling process is crucial for partially decoupling dimensional changes of wood from moisture uptake. The laser drilling process introduced artificial channels and created interconnected structures. These channels opened the wood fibers, facilitating more rapid and efficient moisture exchange, resulting in a more uniform moisture distribution throughout the wood. The laser-drilled channels resulted in localized volume changes around the channels as they disrupted the continuity of the wood fibers and provided local space for the wood to expand during moisture uptake, leading to fewer global dimensional changes. Moreover, the laser drilling process accommodates space for further chemical modification. By inner cell wall coating with MOF particles, we significantly increased the moisture uptake yet not on the expenses of dimensional stability. During the GR ratio tomography measurement, the MOF layer showed a barrier effect to delay water entering the cell wall and reduced swelling by storing water in the MOFs during the water adsorption process in GR-1 measurement. In the following water desorption process, the MOFs functioned as a moisture reservoir to slowly release water in GR-2 measurement. Utilizing the synergy effect between the laser drilling process and cell wall coating by MOFs suggests a promising approach to

This journal is © The Royal Society of Chemistry 2025

J. Mater. Chem. A, 2025, **13**, 6364–6375 | **6373**

increase the moisture uptake of wood composite and limit dimensional changes.

Data availability

The data supporting this article have been included as part of the ESI.† Further information and requests for data and resources will be fulfilled by the lead contact: Dr Yong Ding (yoding@ethz.ch).

Author contributions

Yong Ding: conceptualization, project administration, formal analysis, data curation, investigation, writing – original draft, and writing – review & editing. Mahdieh Shakoorioskooie: formal analysis, data curation, investigation, writing – original draft, and writing – review & editing. David Mannes: data curation. Zhidong Zhang: writing – review & editing. Dmitry Chernyshov: data curation and writing – review & editing. Ingo Burgert: writing – review & editing.

Conflicts of interest

The authors declare no competing interests.

Acknowledgements

Notes and references

1 Y. D. Kuang, C. J. Chen, S. M. He, E. M. Hitz, Y. L. Wang, W. T. Gan, R. Y. Mi and L. B. Hu, *Adv. Mater.*, 2019, **31**, 1900498.
2 F. Chen, A. S. Gong, M. Zhu, G. Chen, S. D. Lacey, F. Jiang, Y. Li, Y. Wang, J. Dai, Y. Yao, J. Song, B. Liu, K. Fu, S. Das and L. Hu, *ACS Nano*, 2017, **11**, 4275–4282.
3 C. Chen, Y. Zhang, Y. Li, J. Dai, J. Song, Y. Yao, Y. Gong, I. Kierzewski, J. Xie and L. Hu, *Energy Environ. Sci.*, 2017, **10**, 538–545.
4 Q. Y. Wu, C. W. Wang, R. L. Wang, C. J. Chen, J. L. Gao, J. Q. Dai, D. P. Liu, Z. W. Lin and L. B. Hu, *Adv. Energy Mater.*, 2020, **10**, 1902590.
5 T. Li, X. Zhang, S. D. Lacey, R. Y. Mi, X. P. Zhao, F. Jiang, J. W. Song, Z. Q. Liu, G. Chen, J. Q. Dai, Y. G. Yao, S. Das, R. G. Yang, R. M. Briber and L. B. Hu, *Nat. Mater.*, 2019, **18**, 608–613.
6 D. W. Zhao, Y. Zhu, W. K. Cheng, G. W. Xu, Q. W. Wang, S. X. Liu, J. Li, C. J. Chen, H. P. Yu and L. B. Hu, *Matter*, 2020, **2**, 390–403.
7 T. Li, S. X. Li, W. Q. Kong, C. J. Chen, E. Hitz, C. Jia, J. Q. Dai, X. Zhang, R. Briber, Z. Siwy, M. Reed and L. B. Hu, *Sci. Adv.*, 2019, **5**, eaau4238.
8 M. Vidiella del Blanco, E. J. Fischer and E. Cabane, *Adv. Mater. Interfaces*, 2017, **4**, 1700584.

9 C. Goldhahn, M. Schubert, T. Lüthi, T. Keplinger, I. Burgert and M. Chanana, *ACS Sustain. Chem. Eng.*, 2020, **8**, 7205–7213.
10 T. Keplinger, E. Cabane, J. K. Berg, J. S. Segmehl, P. Bock and I. Burgert, *Adv. Mater. Interfaces*, 2016, **3**, 6.
11 Y.-T. Li, H. Chen, R. Deng, M.-B. Wu, H.-C. Yang and S. B. Darling, *ACS Appl. Mater. Interfaces*, 2021, **13**, 33713–33721.
12 Y. Ding, K. K. Tu, I. Burgert and T. Keplinger, *J. Mater. Chem. A*, 2020, **8**, 22001–22008.
13 R. Mehrkhah, E. K. Goharshadi and M. Mohammadi, *J. Ind. Eng. Chem.*, 2021, **101**, 334–347.
14 C. Hu, W. Li, H.-Y. Zhao, C. Li, Z.-Y. Ma, L. Hao, Y. Pang, Z.-Z. Yu and X. Li, *Chem. Eng. J.*, 2023, **460**, 141622.
15 L. Shi, M. Zhang, X. Du, B. Liu, S. Li and C. An, *J. Mater. Sci.*, 2022, **57**, 16317–16332.
16 M. G. Qin, P. M. Hou, Z. M. Wu and J. T. Wang, *Build. Environ.*, 2020, **169**, 106581.
17 Z. M. Wu, M. H. Qin and M. J. Zhang, *Energy Build.*, 2018, **174**, 254–261.
18 M. Qin, *1st International Conference on Moisture in Buildings*, 2021.
19 T. T. Yang, K. R. Zhang, C. T. Mei, E. N. Ma and J. Z. Cao, *Wood Sci. Technol.*, 2022, **56**, 703–720.
20 T. T. Yang and E. Ma, *Int. J. Polym. Sci.*, 2016, **2016**, 2454610.
21 O. F. Osanyintola and C. J. Simonson, *Energy Build.*, 2006, **38**, 1270–1282.
22 T. Alapieti, R. Mikkola, P. Pasanen and H. Salonen, *Eur. J. Wood Wood Prod.*, 2020, **78**, 617–634.
23 K. Nore, A. Q. Nyrud, D. Kraniotis, K. R. Skulberg, F. Englund and T. Aurlien, *Sci. Technol. Built Environ.*, 2017, **23**, 512–521.
24 Y. Ran, J. Li, S. Zhang, J. Wang, Y. Huang, W. Wang and J. Cao, *Chem. Eng. J.*, 2024, **488**, 150814.
25 Y. Ding, C. H. Dreimol, R. Zboray, K. K. Tu, S. Stucki, T. Keplinger, G. Panzarasa and I. Burgert, *Mater. Horiz.*, 2023, **10**, 257–267.
26 K. Tu, Z. Zhang, C. H. Dreimol, R. Günther, R. Zboray, T. Keplinger, I. Burgert and Y. Ding, *Mater. Horiz.*, 2024, **11**, 5786–5797.
27 A. Patera, D. Derome, M. Griffa and J. Carmeliet, *J. Struct. Biol.*, 2013, **182**, 226–234.
28 M. Libralato, A. De Angelis, P. D'Agaro, G. Cortella, M. Qin and C. Rode, *J. Phys.: Conf. Ser.*, 2021, **2069**, 012043.
29 R. Sargent, *J. Wood Sci.*, 2019, **65**, 36.
30 K. Tu, X. Wang, L. Kong, H. Chang and J. Liu, *RSC Adv.*, 2016, **6**, 701–707.
31 K. Tu, X. Wang, L. Kong and H. Guan, *Mater. Des.*, 2018, **140**, 30–36.
32 C. Wang and C. Piao, *Wood Fiber Sci.*, 2011, 41–56.
33 D. C. Mannes, *Non-destructive testing of wood by means of neutron imaging in comparison with similar methods*, PhD Thesis, ETH Zurich, 2009.
34 W. Sonderegger, D. Mannes, A. Kaestner, J. Hovind and E. Lehmann, *Holzforschung*, 2015, **69**, 87–95.
35 M. Sedighi-Gilani, M. Griffa, D. Mannes, E. Lehmann, J. Carmeliet and D. Derome, *Int. J. Heat Mass Transfer*, 2012, **55**, 6211–6221.

6374 | *J. Mater. Chem. A*, 2025, **13**, 6364–6375

This journal is © The Royal Society of Chemistry 2025

36 D. Mannes, W. Sonderegger, S. Hering, E. Lehmann and P. Niemz, *Holzforschung*, 2009, **63**, 589–596.

37 W. Sonderegger, M. Glaunsinger, D. Mannes, T. Volkmer and P. Niemz, *Eur. J. Wood Wood Prod.*, 2015, **73**, 793–799.

38 H. Li, Y. Xia, W. Zeng, H. Zhan, G. Sun, C. Huang, J. Mei, B. Lv, Y. Huang and S. Lu, *J. Mater. Chem. A*, 2024, **12**, 27570–27576.

39 M. E. Potter, A. E. Oakley, J. J. Le Brocq, L. N. Riley, M. Carravetta, S. M. King, C. M. Doherty, B. D. Vandegehuchte and R. Raja, *J. Mater. Chem. A*, 2023, **11**, 22822–22834.

40 A. Kaestner, B. Münch, P. Trtik and L. Butler, *Opt. Eng.*, 2011, **50**, 123201–123209.

41 Y. Ding, G. Panzarasa, S. Stucki, I. Burgert and T. Keplinger, *ACS Sustainable Chem. Eng.*, 2022, **10**, 5517–5525.

42 H. Zhao, Q. Li, Z. Wang, T. Wu and M. Zhang, *Microporous Mesoporous Mater.*, 2020, **297**, 110044.

43 V. Dyadkin, P. Pattison, V. Dmitriev and D. Chernyshov, *J. Synchrotron Radiat.*, 2016, **23**, 825–829.

44 D. R. Black, D. Windover, A. Henins, J. Filliben and J. P. Cline, *Powder Diffr.*, 2011, **26**, 155–158.

45 D. Mannes, F. Schmid, T. Wehmann and E. Lehmann, *Phys. Procedia*, 2017, **88**, 200–207.

46 M. Shakoorioskooie, M. Griffa, A. Leemann, R. Zboray and P. Lura, *Supplementary data/materials for the article:"Alkali-silica reaction products and cracks: X-ray micro-tomography-based analysis of their spatialtemporal evolution at a mesoscale*, Zenodo, 2021.

47 M. Shakoorioskooie, M. Griffa, A. Leemann, R. Zboray and P. Lura, *Cem. Concr. Res.*, 2021, **150**, 106593.

48 R. M. Mahamood, in *Laser Metal Deposition Process of Metals, Alloys, and Composite Materials*, Springer-Verlag London Ltd, Godalming, 2018, pp. 11–35, DOI: **10.1007/978-3-319-64985-6_2**.

49 N. X. Zhu, Z. W. Wei, C. X. Chen, X. H. Xiong, Y. Y. Xiong, Z. Zeng, W. Wang, J. J. Jiang, Y. N. Fan and C. Y. Su, *Angew. Chem., Int. Ed.*, 2022, **61**, e202112097.

50 B. Lerma-Berlanga, C. R. Ganivet, N. Almora-Barrios, S. Tatay, Y. Peng, J. Albero, O. Fabelo, J. Gonzalez-Platas, H. Garcia, N. M. Padial and C. Marti-Gastaldo, *J. Am. Chem. Soc.*, 2021, **143**, 1798–1806.

51 A. J. Rieth, A. M. Wright, S. Rao, H. Kim, A. D. LaPotin, E. N. Wang and M. Dinca, *J. Am. Chem. Soc.*, 2018, **140**, 17591–17596.

52 H. Furukawa, F. Gandara, Y. B. Zhang, J. C. Jiang, W. L. Queen, M. R. Hudson and O. M. Yaghi, *J. Am. Chem. Soc.*, 2014, **136**, 4369–4381.

53 R. G. AbdulHalim, P. M. Bhatt, Y. Belmabkhout, A. Shkurenko, K. Adil, L. J. Barbour and M. Eddaoudi, *J. Am. Chem. Soc.*, 2017, **139**, 10715–10722.

54 D. Ma, P. Li, X. Y. Duan, J. Z. Li, P. P. Shao, Z. L. Lang, L. X. Bao, Y. Y. Zhang, Z. G. Lin and B. Wang, *Angew. Chem., Int. Ed.*, 2020, **59**, 3905–3909.

55 J. W. Zhang, P. Li, X. N. Zhang, X. J. Ma and B. Wang, *ACS Appl. Mater. Interfaces*, 2020, **12**, 46057–46064.

56 Z. J. Chen, P. H. Li, X. Zhang, P. Li, M. C. Wasson, T. Islamoglu, J. F. Stoddart and O. K. Farha, *J. Am. Chem. Soc.*, 2019, **141**, 2900–2905.

57 N. M. Padial, E. Q. Procopio, C. Montoro, E. Lopez, J. E. Oltra, V. Colombo, A. Maspero, N. Masciocchi, S. Galli, I. Senkovska, S. Kaskel, E. Barea and J. A. R. Navarro, *Angew. Chem., Int. Ed.*, 2013, **52**, 8290–8294.

58 C. D. Hatch, J. S. Wiese, C. C. Crane, K. J. Harris, H. G. Kloss and J. Baltrusaitis, *Langmuir*, 2012, **28**, 1790–1803.

59 H. Xu, M. Zu, H. Cheng, D. Liu and W. Xie, *Angew. Chem., Int. Ed.*, 2022, **5**, 2896–2905.

60 J. Canivet, J. Bonnefoy, C. Daniel, A. Legrand, B. Coasne and D. Farrusseng, *New J. Chem.*, 2014, **38**, 3102–3111.

61 D. Y. Hong, Y. K. Hwang, C. Serre, G. Ferey and J. S. Chang, *Adv. Funct. Mater.*, 2009, **19**, 1537–1552.

This journal is © The Royal Society of Chemistry 2025

J. Mater. Chem. A, 2025, **13**, 6364–6375 | **6375**